Nanoscale Advances

ROYAL SOCIETY OF CHEMISTRY

COMMUNICATION

View Article Online
View Journal | View Issue

Cite this: *Nanoscale Adv.*, 2026, **8**, 1836

Received 1st November 2025
Accepted 5th February 2026

DOI: 10.1039/d5na01015b

rsc.li/nanoscale-advances

Green synthesis of bio-compatible carboxylate-functionalized carbon layers of 4 to 26 nm thickness on gold plasmonic nanoparticles

Mike Rozenberg,[a] Avi Huri,[a] Eli Varon,[b] Anya Muzikansky,[a] Orit Shefi,[b] Eli Sloutskin[c] and David Zitoun*[a]

Polycrystalline spherical plasmonic gold nanoparticles (GNPs) were coated with carboxylate-functionalized carbon layers with unprecedented thinness down to 4 nm, tunable between 4 and 26 nm, *via* a hydrothermal approach using glucose, fructose or sucrose as carbon sources. This synthetic approach allows for the formation of conformally coated GNPs with well-controlled carbon-layer thicknesses as a function of initial carbon source concentration. These carbon coated GNPs exhibit plasmon resonance at ~545 nm and have an increased absorbance at 400 nm, which is found to correlate linearly with the thickness of the carbon layer with a squared Pearson correlation coefficient of 0.94. The coated GNPs are shown to be bio-compatible through incubation with SH-SY5Y cells with varying carbon coating thicknesses, without changes in cellular morphology and exhibiting increased proliferation with no notable differences when compared with the control or citrate capped GNPs, over 48 hours.

1. Introduction

Gold nanoparticles (GNPs) have become the subject of interest in many fields due to their unique optical properties[1,2] and biocompatibility.[3] These properties make them suitable for a wide range of applications, from imaging,[4] sensing[5,6] and drug delivery[7] to photo-thermal treatments,[8] solar cells[9] and catalysis.[10] In particular, the GNPs display Localized Surface Plasmon Resonance (LSPR), a collective oscillation of the conduction band electrons within a confined structure, resulting from light irradiation at appropriate wavelengths, which can be tuned by varying the composition, shape, size and dielectric environment surrounding the nanoparticles, allowing for optical property tunability or preservation, depending on the desired application.[11]

While generally considered biocompatible,[12] surface engineering is often employed to either improve upon it, maintain it post synthesis (especially when cytotoxic reagents are used), or to introduce additional chemical functionality for drug delivery or addition of a particular desired action.[13,14] Among the various methods used to modify the surface chemistry of nanoparticles are direct ligand exchange (commonly with polyethylene glycol for bio-compatibility),[12] Layer-By-Layer (LBL) grafting of polymers,[15] silica,[16] or Metal–Organic-Frameworks (MOFs) by seeded growth,[17] and protein coupling.[18] Proper thickness control is difficult to achieve by only one method, especially when both thin (below 5 nm) and thick (beyond 20 nm) coatings are desired, depending on the application.[14,16,19,20]

Glucose-derived hydrochars have been shown to coat spherical gold nanoparticles by a single-step hydrothermal reaction using the precursor gold complex along with glucose to produce a micron-sized coating around spherical GNPs.[21] More recently, similar glucose-derived hydrochar layers on GNPs with varying thicknesses from 10 nm to 25 nm have been used to negate the cytotoxic effects of CTAB moieties surrounding gold nanorods. Nevertheless, the synthesis yields coated GNPs with a very large hydrodynamic diameter (~165 nm)[22,23], due to sintering of the carbon layers of multiple GNPs. The resulting coated GNPs are less optimal for cellular uptake and drug delivery applications, when usually the target is around ~50 nm for optimal cellular uptake.[24]

In this research, GNPs have been directly coated with sugar (mainly glucose, with fructose or sucrose used in controlled synthesis) without an additional surfactant like CTAB by hydrothermal synthesis to yield GNPs coated with carbon (Au@C) with an hydrodynamic radius as low as 31.3(±0.8) nm compared to the pristine GNPs with an 18.3(±0.1) nm hydrodynamic radius.

[a]*Department of Chemistry, Bar-Ilan Institute of Nanotechnology and Advanced Materials (BINA), Bar-Ilan University, Ramat Gan 5290002, Israel. E-mail: David.Zitoun@biu.ac.il*

[b]*Faculty of Engineering, Bar-Ilan Institute of Nanotechnology & Advanced Materials (BINA), Bar-Ilan University, Ramat Gan 529002, Israel*

[c]*Physics Department, Institute of Nanotechnology & Advanced Materials (BINA), Bar-Ilan University, Ramat Gan 529002, Israel*

2. Experimental section

2.1. Materials synthesis

2.1.1 Reagents. Sodium citrate tribasic dihydrate (>99%, ACROS ORGANICS), hydrogen tetrachloroaurate(III) trihydrate (99.9% Au, System Chemicals), double-distilled water (ddH_2O, 18 MΩ cm^{-1}, Millipore), buffer solution pH 10 (AVS TITRINORM, VWR CHEMICALS), D-glucose, D-fructose and sucrose (>99%) were all obtained from Sigma Aldrich.

2.1.2 Preparation of Au nanoparticles. 197 mg of hydrogen tetrachloroaurate(III) trihydrate is added to 950 ml of double distilled water under stirring over a hot plate and brought to boiling. 50 ml of a 1% w/w% trisodium citrate aqueous solution is injected in one shot to the boiling solution and covered with aluminum foil; the reaction is run for 20 minutes on the hot plate. Upon observation of the standard red color of the solution, the reaction vessel is removed from the hot plate, put aside to rest and cool to room temperature for 1 day prior to use. The particles are stored afterwards in the fridge.

2.1.3 Preparation of Au@C nanoparticles. To a Teflon or glass-lined 25 ml stainless steel autoclave, 10 ml of the Au@citrate particle solution are added. 0.1 ml of the buffer solution is added in one shot, and a standard volume of 0.25 ml of a 0.2 M aqueous glucose (or fructose/sucrose) solution are added, and the volume is adjusted to 12.5 ml; if a higher concentration is desired, a larger volume of the carbon source solution is then added. The autoclave is then sealed, lightly shaken and placed inside a furnace at 165–170 °C for 12 hours.

Once the autoclave containing the particle solution is cooled to room temperature, it is opened and the contents are transferred to a centrifuge tube. The particles are washed twice, with double distilled water, for 45 minutes at 13k rpm each round.

2.2. Materials characterization

The morphology, size, and distribution of the nanoparticles were imaged using a JEOL JEM 1400 transmission electron microscope (TEM) operated at 120 kV and a JEOL JEM F200 high-resolution TEM (HR-TEM) operated at 200 kV. Carbon thickness measurements were performed using ImageJ software. The samples were prepared *via* drop-casting on 200 mesh or 300 mesh copper@formvar electron microscopy grids.

X-ray photoelectron spectroscopy (XPS) was used to characterize the functionality of the carbon layer surrounding the particles and confirm the conformal nature of the coating process across the colloidal sample. A Nexsa X-ray photoelectron spectrometer system (Thermo Scientific) with a monochromated Al Ka X-ray source was used. Measurements were taken at room temperature under high vacuum (<3.0×10^{-9} torr). A spot size of 400 μm was used with a pass energy of 40 eV. The samples were prepared by drop-casting on Cu tape for the survey and high-resolution data. The etching experiments were performed by Ar^+ sputter etching for 60 s and 150 s at low and high currents at 4 kV.

Optical characterization of the Au@citrate and Au@C nanoparticles was performed using a Shimadzu UV-1280 UV-vis-NIR spectrophotometer.

DLS measurements were performed using a Photocor™ goniometer-based setup (Photocor Instruments, Tallinn, Estonia), with time-averaged scattered intensity autocorrelation, $(2)(\delta t) = \langle I(t)I(t+\delta t)\rangle$, measured over a wide range of scattering angles θ, where the wave vector is $q = (4\pi n/\lambda)\sin(\theta/2)$, n is the refractive index of water and $\lambda = 633$ nm is the radiation wavelength. We then fit the autocorrelation by a simple exponential decay: $g^{(2)}(\delta t) = B + \beta \exp(-2\Gamma\delta t)$, where the background B, the contrast β, and the decay rate $\Gamma(q)$ are fitting parameters. The diffusion rate of the particles is then obtained as the linear slope of $\Gamma(q^2)$; see the main text. The present analysis, where DLS data obtained over a wide range of scattering angles are analyzed at once, is generally more accurate than the simpler single-θ DLS measurements.

2.3. Cell biocompatibility

The IncuCyte® SX5 Live-Cell Analysis System (Sartorius, Ann Arbor, MI, USA) was used to acquire label-free, high-throughput, phase-contrast images. Human neuroblastoma cells, SH-SY5Y (ATCC), were grown in tissue culture flasks (Greiner, Stroudwater, UK) containing high glucose Dulbecco's modified Eagle's medium (DMEM, Sigma-Aldrich, St. Louis, MO, USA). The medium was supplemented with 10% fetal bovine serum (FBS), 1% L-glutamine, 1% penicillin–streptomycin, and 0.2% amphotericin (Biological Industries, Beit-Haemek, Israel). The cells were incubated at 37 °C in a humidified atmosphere with 5% CO_2/95% air and were subcultured twice a week by adding 5 ml of trypsin upon reaching a confluence of ~70%. The cell cultures were monitored daily for up to a week using light microscopy (Leica DM IL LED; Leica Microsystems, Wetzlar, Germany). The system enables continuous real-time monitoring of live cells under optimal culture conditions while avoiding the phototoxic and cytotoxic effects of fluorescence-based approaches. SH-SY5Y cells (ATCC) were incubated in a 12-well culture plate and treated with either uncoated gold nanoparticles or gold nanoparticles coated with carbon layers of 4.11 nm, 8.53 nm, 13.87 nm, and 26.23 nm thicknesses. 24 μl of the washed particles were added to 1 ml of cells and the cell plates were then placed inside the IncuCyte® SX5 system. Images were obtained in real time using the IncuCyte® SX5 instrument with phase-contrast imaging according to the manufacturer's protocol. Time-lapse images were collected every 4 h for a period of 48 hours using a 10× objective, which provides detailed imaging while allowing observation of a large portion of the sample over an extended period without causing harm to the cells, as recommended by the manufacturer's protocol.

3. Results and discussion

3.1. Carbon shell thickness and hydrodynamic radius

GNPs were synthesized *via* the standard (modified Turkevich) citrate reduction method to yield Au NPs.[25] The GNPs are spherical in shape with a particle size distribution of 16.3(±1.4) nm (Fig. 1a) and stabilized only by citrate without any other stabilizer. An aqueous solution of the carbon source (glucose,

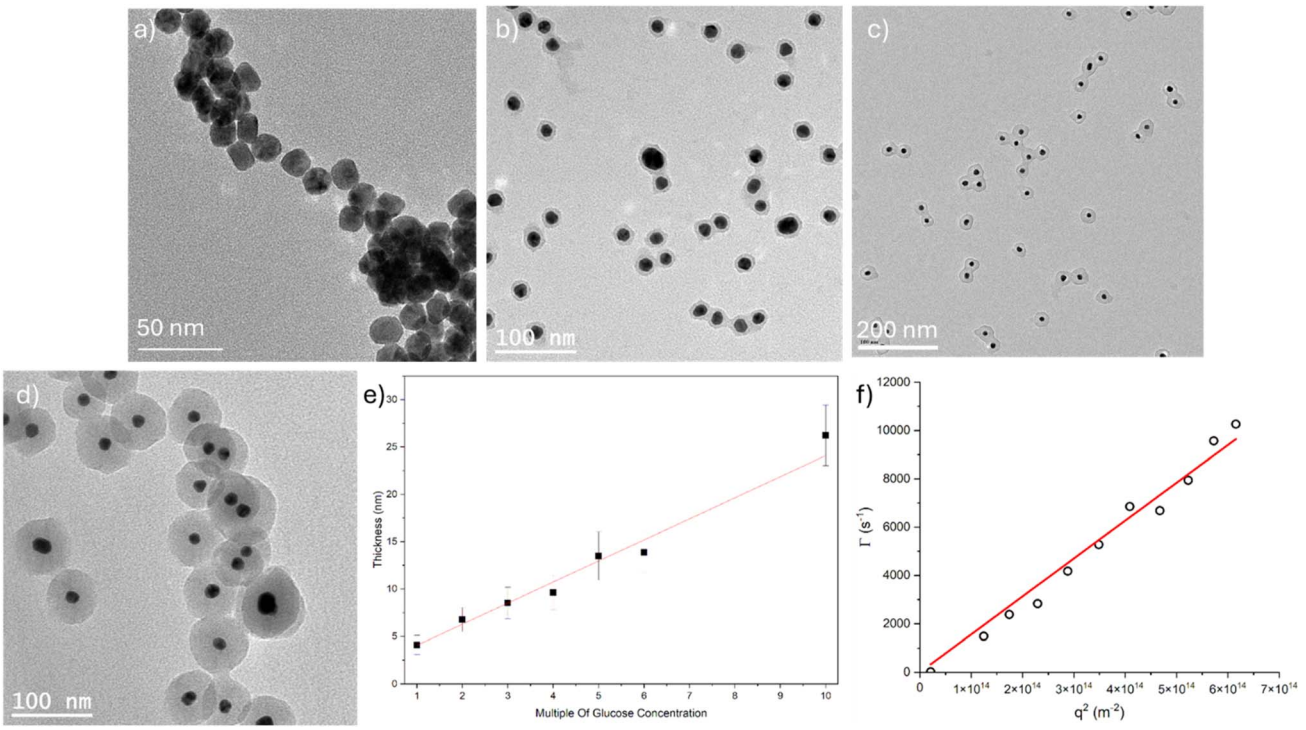

Fig. 1 TEM images of (a) Au NPs and Au@C NPs synthesized from glucose and coating thicknesses of (b) 4.1(±0.99) nm, (c) 13.5(±1.2 nm) and (d) 26.2(±3.2 nm); (e) thickness of the carbon coating scaled linearly with increasing multiples of glucose concentration and (f) particle sizing of Au@C nanoparticles with a coating thickness of 4.1 ± 0.99 nm by DLS.

fructose or sucrose) and buffer are added, and the final volume is adjusted with water to match half of the volume of the Teflon/glass-lined autoclave (Table S1). The autoclave is then sealed and placed in an oven at 165 °C for 12 hours. The resulting particles are washed twice with doubly deionized water and are then used and characterized.

The carbon shell conformally coats the GNPs with a thin layer of 4.1(±0.99) nm (Fig. 1b). The thickness is tunable as a function of increasing sugar content (see Fig. 1e), with a shell thickness of 13.5(±1.2 nm) and 26.2(±3.2 nm), as shown on TEM images in Fig. 1c and d, respectively. The experimental conditions are summarized in Table S1. In the following sections, the samples are named Au@C_*X* nm for a *X* nm thin layer. The same reaction conditions are applied on different sugars used as carbon precursors. Au@C synthesized from fructose tend to exhibit more fusion between the carbon shells but retain the same carbon thickness as those synthesized from glucose under the same reaction conditions (4.11 ± 0.99 nm and 3.86 ± 0.71 nm for glucose and fructose respectively) (Fig. S2a). Au@C from sucrose displays an increased thickness of the carbon shell (6.83 ± 1.20 nm) compared to glucose but does not exhibit more fusion (Fig. S2b).

Therefore, the systematic study was carried out using glucose as the carbon source. Fig. S3 displays the TEM images of Au@C_4 nm (Fig. S3a), Au@C_7 nm (Fig. S3b), Au@C_8 nm (Fig. S3c), Au@C_10 nm (Fig. S3d), Au@C_13 nm (Fig. S3e), and Au@C_14 nm (Fig. S3f).

DLS was used to ascertain the hydrodynamic diameter of the prepared particles ,[26] by plotting Γ (autocorrelation decay rate) as a function of the wave vector q^2 (Fig. 1f); a linear scaling is observed, indicative of low polydispersity of the GNPs. The diffusion coefficient D is the slope and is found to be $D = \Gamma/q^2 = 1.56 \times 10^{-11}$ m^2 s^{-1}. The hydrodynamic diameter of the particles is then found using $d = k_B T/3\pi\eta D = 31.3(\pm 0.8)$ nm (η: water dynamic viscosity), which is slightly higher than 26.9(±2.3) nm observed by TEM. The apparent size discrepancy between TEM and DLS indicates slight sintering of the particles, which is observed by TEM (Fig. S2a). For reference (Fig. S1), the Au NP hydrodynamic diameter is 18.3(±0.1) nm. A diameter of 58.6(±0.6) nm is obtained for Au@C_10 nm, which is near the ideal ~50 nm mark for optimal cellular uptake.[24]

The role of the buffer is mainly to retain the colloidal stability of the particles post-washing, as we found that otherwise the particles tend to aggregate; therefore, we add the buffer in the beginning to directly move towards washing post-synthesis. The particles were produced without the use of cytotoxic cetylammonium bromide (CTAB), which was claimed to be necessary for the coating of gold nanoparticles,[22,23] allowing production of GNPs with citrate ions as the initial stabilizer resulting in fully bio-compatible nanoparticles by design of both the synthetic process and product. The process, mechanism and kinetics of hydrothermal carbonization of glucose, fructose and sucrose to form carbonized micro and nanospheres have been extensively studied,[21,27–29] and involve the eventual transition of the carbon source into 5-hydroxymethylfurfural (HMF), after which HMF undergoes condensation, polymerization and aromatization to form the hydrochar. When Au nanoparticles are introduced, they act as nucleation

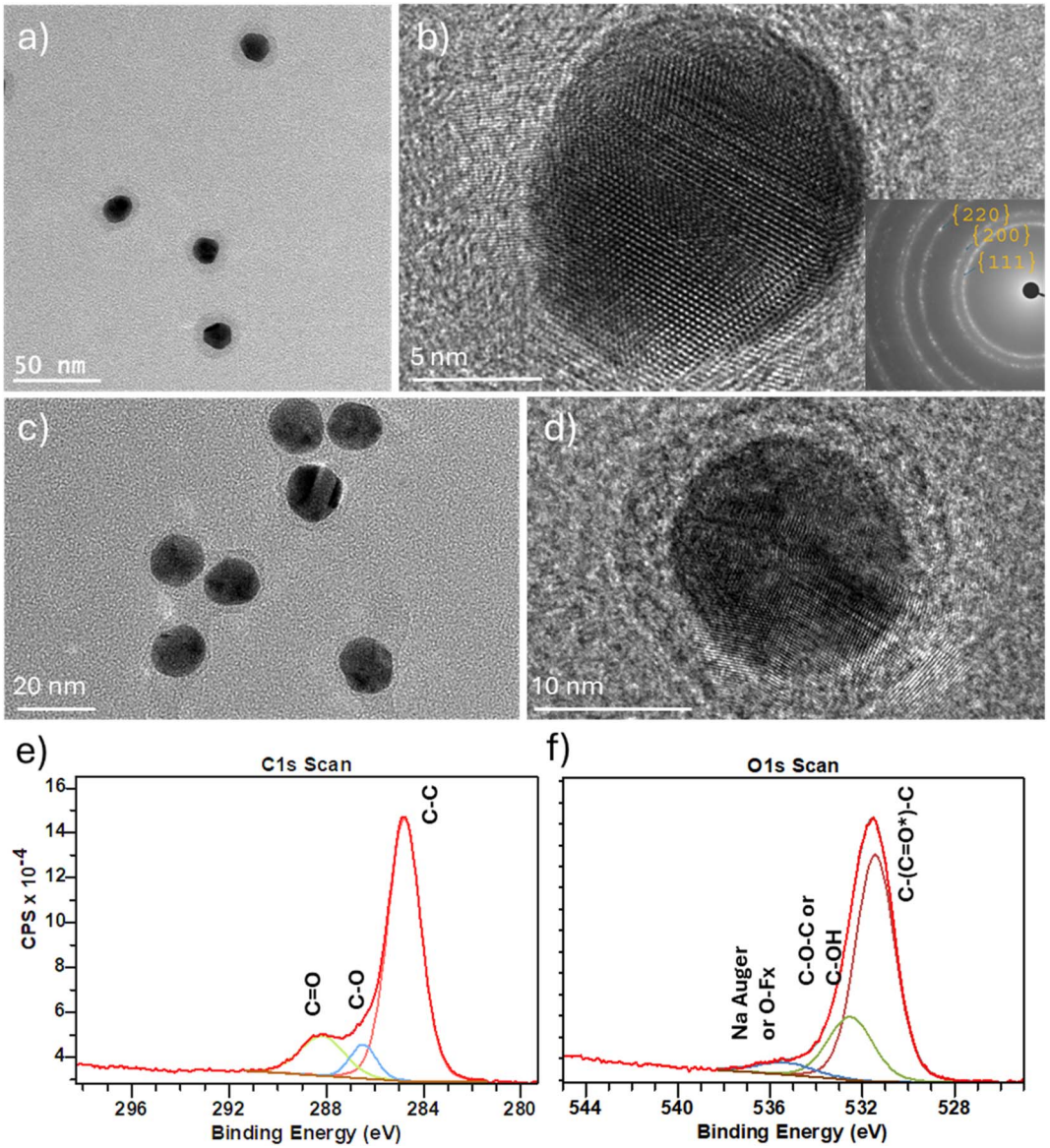

Fig. 2 (a) TEM image of Au@C_4 nm, (b) HR-TEM image of Au@C_4 nm and the SAED inset indicating a polycrystalline structure; HR-TEM images of Au@C_4 nm prepared with (c) fructose and (d) sucrose as the carbon sources instead of glucose at the same standard concentration; XPS spectra of the Au@C_4 nm made from glucose for (e) C 1s and (f) O 1s.

sites for the hydrochar formation, resulting in Au@C NPs with a polymerized layer of the carbon source on the outer layer of the GNPs.[21]

The resulting Au@C_4 nm are well dispersed on the TEM grid (Fig. 2a) and highly crystalline (Fig. 2b). The synthesis can also be done with alternative sugars as carbon sources, such as fructose (Fig. 2c) and sucrose (Fig. 2d) to yield similar carbon coated Au nanoparticles (Fig. S2). The fructose coated nanoparticles have a ~4 nm thickness while the sucrose coated nanoparticles have a ~7 nm thickness. Sucrose is a disaccharide composed of both glucose and fructose monomers and breaks down during the hydrothermal process, explaining why at the same concentration the resulting thickness is overall larger compared to the monosaccharaides. Carbonized fructose coated nanoparticles appear to exhibit a higher degree of overall fusion between the particles (Fig. S2a).

3.2. Carbon functional surface

Au@C nanoparticles display a shell that could be functionalized by standard organic reactions *via* the carboxylate groups[30] on the carbon coating as confirmed by XPS with C 1s peaks at 288.24 eV for the C═O bond and 286.46 eV for the C–O bond, and O 1s peaks at 532.45 eV for the C–O–C and C–OH bonds and at 531.45 eV for the C–(C═O*)–C bond (Fig. 2e and f).[31]

The thickness of the carbon coating (Fig. S3) can be adjusted based on the initial concentration of glucose added while all other conditions remain the same. We have demonstrated control over the thickness for up to 10 times the initial concentration of glucose to achieve a carbon coating thickness

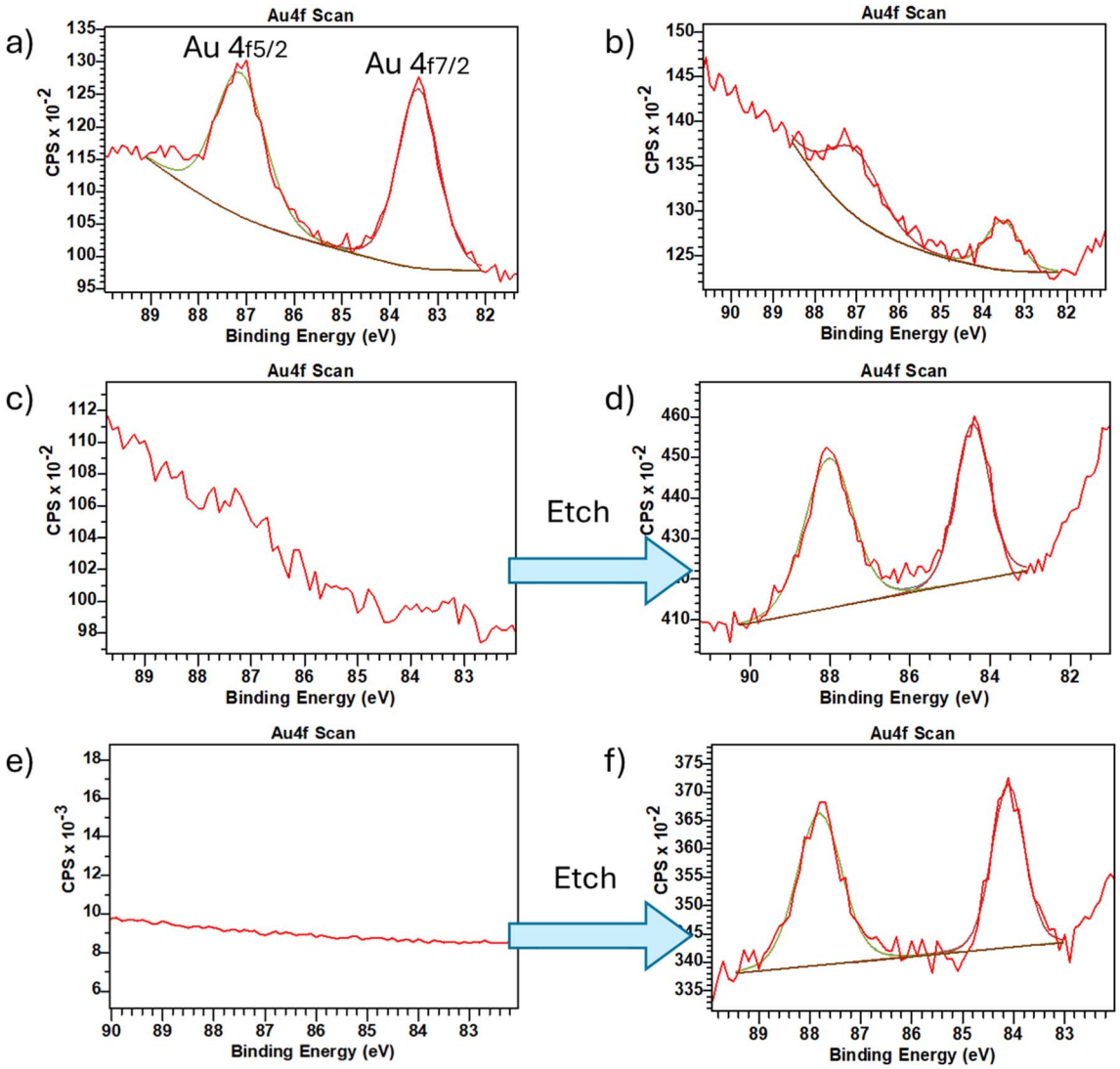

Fig. 3 XPS spectra of the Au 4f orbital of (a) Au@C_4 nm; (b) Au@C_8 nm; (c) Au@C_13 nm and (d) Au@C_13 nm post-etching with Ar^+; (e) Au@C_26 nm and (f) Au@C_26 nm post-etching with Ar^+.

of ~26 nm (Fig. S4a), with the same surface chemistry as indicated by the C 1s and O 1s XPS spectra (Fig. S4), which is consistent for other thicknesses as well (Fig. S5). As expected with a thick layer, the XPS signal for the Au core has disappeared (Fig. 3e). The absence of the Au 4f signal in the XPS spectra demonstrates the conformal coating of the carbon across the sample, due to the limited of penetrative capability of the XPS device at such depths (or thickness, in our case). To confirm, we have compared the XPS spectra of Au 4f in Au@C_4 nm, Au@C_8 nm, Au@C_13 nm, and Au@C_26 nm (Fig. 3a, b, c and e, respectively). We observed that the signal intensity reduces with increasing thickness of the carbon coating,[32] already masking the Au 4f peaks at a coating thickness of 13 nm (Fig. 3c). We can uncover the Au 4f signal (Fig. 3d and f), although it is mildly oxidized due to the nature of the process, as observed by a positive shift of both the Au $4f_{7/2}$ and $4f_{5/2}$ peaks to higher values from 83.33 eV and 87.12 eV (which is slightly negatively charged) to 84.4 eV and 88.16 eV, respectively, confirming the presence of a gold core. This disappearance of Au 4f peaks at increasing carbon thicknesses indicates that, beyond the TEM images shown, the entire GNPs are conformally coated with the carbonized-polymerized glucose; as otherwise, we would still be able to observe the Au peaks, regardless of the observed thickness of the carbon in the TEM images. This holds true for both the Au@C_13 nm and Au@C_26 nm samples.

3.3. Optical properties and biocompatibility

The spherical citrate capped GNPs exhibit a plasmon resonance at 519 nm, whilst particles coated with a carbon layer exhibit their plasmon resonance shifted to 545 nm (Fig. 4a). The red shift results from the increase in the surrounding dielectric environment constant around the particles coated with the carbon layer.[33] As the dielectric constant of a carbon layer is higher than that of water,[23,34] a red shift of the plasmon

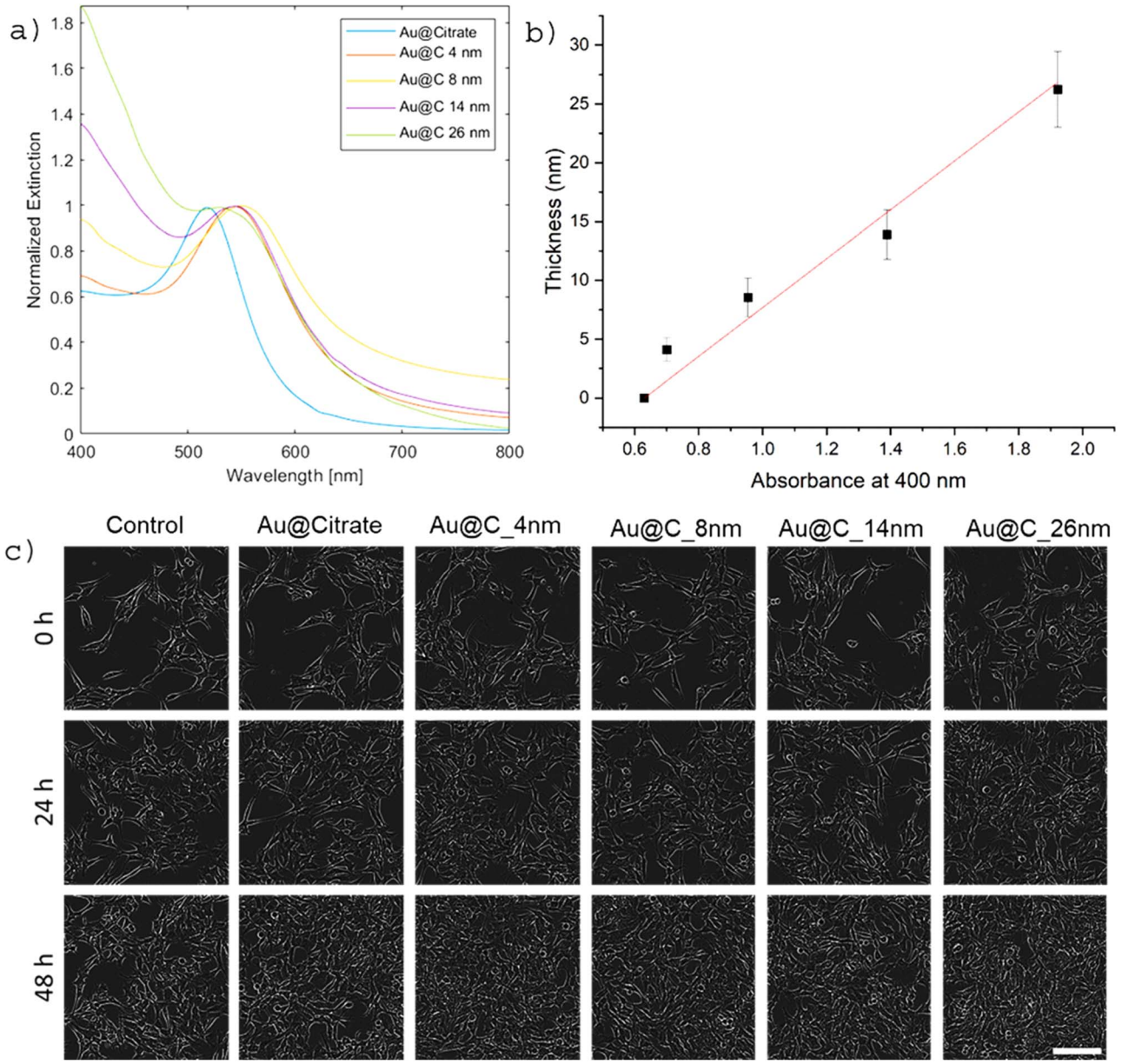

Fig. 4 (a) UV-vis spectra of GNPs with various carbon coating thicknesses from the glucose precursor, (b) linear correlation between the thickness of the carbon layer and the relative absorbance at 400 nm (c) phase-contrast images of SH-SY5Y cells, either untreated, incubated with Au NPs, or with Au@C_4 nm, Au@C_8 nm, Au@C_13.87 nm Au@C_26 nm, acquired at 0, 24, and 48 h. Scale bar: 200 μm.

resonance is observed based on Mie theory.[35] The increased absorbance below 489 nm in the Au@C NPs, relative to the innate d–d band transition absorbance observed in the Au NPs,[9] is due to additional absorbance by the carbonized glucose layer itself,[29,36] caused by the aromatization of the carbon. The carbon layer thickness is found to be linearly correlated to the relative absorbance at 400 nm (Fig. 4b) with a squared Pearson correlation coefficient (sPCC) of 0.94, *via* the relation thickness = $20.78 \times \text{Abs} - 13.09$.

To examine the biocompatibility of our carbon coating and assess whether variations in its thickness are non-toxic, we incubated SH-SY5Y cells with either uncoated GNPs (Au@citrate) or coated GNPs Au@C_4 nm, Au@C_8 nm, Au@C_14 nm, Au@C_26 nm for 48 h and compared to untreated cells. Representative phase-contrast images of SH-SY5Y cells (background set to black to enhance contrast) show a typical healthy neuronal-like morphology under all conditions, with well-adhered cells, intact borders, and preserved neurite-like extensions (Fig. 4c). As displayed, no signs of stress or cytotoxicity are observed, such as rounding, detachment, or membrane blebbing. Live imaging over 48 hours was performed to evaluate cell viability by quantifying proliferation (cell counts and confluency) and monitoring potential morphological changes (Fig. S6). Under all conditions, confluency increased over time and cell numbers rose in a comparable manner, indicating sustained proliferation. These results demonstrate that

differences in the carbon layer do not affect SH-SY5Y cell viability or growth. In conclusion, we found that untreated cells grew similarly to cells treated with either citrate coated or carbon-coated gold nanoparticles across all tested thicknesses, with no apparent differences in cellular morphology and demonstrated increased proliferation, as indicated by higher cell density within the plate.

4. Conclusions

In summary, gold nanoparticles with carbon coating have been prepared *via* a hydrothermal and green approach using various sugars to produce tunable carbon layers ranging from 4 nm to 26 nm in thickness and without the use of cytotoxic reagents such as CTAB; this demonstrates that other surface chemistries are suitable for carbon coating through this process and potentially removes a ligand exchange step of adding CTAB in future rational design of multi-step synthetic processes. Au@C_4 nm produced with a thin carbon coating displays a hydrodynamic diameter of ~31.3 nm, making it particularly suitable for intra-cellular drug delivery applications. Au@C GNPs possess a functional carboxylate surface chemistry as confirmed *via* XPS. The conformal coating of the carbon layer is confirmed *via* etching-XPS analysis, in which the gold core is revealed when the carbon layer thickness begins to mask its presence and etching is required to observe it, indicating that the carbon layer is covering the entirety of the colloidal system. The Au@C nanoparticles show a plasmon resonance at 545 nm, making them of particular interest for potential applications in photo-thermal and photo-dynamic therapies. The thickness of the carbon coating is found to be linearly correlated with the relative absorbance at 400 nm with sPCC of 0.94. Finally, their bio-compatible nature is apparent as no differences in cellular morphology and rate of proliferation are observed across several carbon layer thicknesses.

Conflicts of interest

There are no conflicts to declare.

Data availability

All the data are available in the supplementary information (SI). Supplementary information is available. See DOI: https://doi.org/10.1039/d5na01015b.

References

1 H. Wang, *Chem. Commun.*, 2025, **61**, 13807–13826.
2 A. Lee, S. Wu, J. E. Yim, B. Zhao and M. T. Sheldon, *ACS Nano*, 2024, **18**, 19077–19085.
3 S.-Y. Hwang and A. R. Tao, *Pure Appl. Chem.*, 2010, **83**, 233–241.
4 L. K. Bogart, G. Pourroy, C. J. Murphy, V. Puntes, T. Pellegrino, D. Rosenblum, D. Peer and R. Lévy, *ACS Nano*, 2014, **8**, 3107–3122.
5 T. C. Lebepe, S. Parani and O. S. Oluwafemi, *Nanomaterials*, 2020, **10**, 1–24.
6 Y. Bao and A. Oluwafemi, *Chem. Commun.*, 2024, **60**, 469–481.
7 M. Yafout, A. Ousaid, Y. Khayati and I. S. El Otmani, *Sci. Afr.*, 2021, DOI: 10.1016/j.sciaf.2020.e00685.
8 J. B. Vines, J. H. Yoon, N. E. Ryu, D. J. Lim and H. Park, *Front. Chem.*, 2019, **7**, 1–16.
9 P. Reineck, D. Brick, P. Mulvaney and U. Bach, *J. Phys. Chem. Lett.*, 2016, **7**, 4137–4141.
10 M. Luna, Á. Cruceira, A. Díaz, J. M. Gatica and M. J. Mosquera, *Environ. Technol. Innov.*, 2023, **30**, 103070.
11 J. Zheng, X. Cheng, H. Zhang, X. Bai, R. Ai, L. Shao and J. Wang, *Chem. Rev.*, 2021, **121**, 13342–13453.
12 M. Kus-liśkiewicz, P. Fickers and I. Ben Tahar, *Int. J. Mol. Sci.*, 2021, DOI: 10.3390/ijms222010952.
13 M. Rozenberg, M. Bárta, A. Muzikansky, M. Zysler, K. Šišková, Y. Mastai and D. Zitoun, *Nanoscale Adv.*, 2024, **6**, 4831–4841.
14 E. Varon, G. Blumrosen, M. Sinvani, E. Haimov, S. Polani, M. Natan, I. Shoval, A. Jacob, A. Atkins, D. Zitoun and O. Shefi, *Int. J. Mol. Sci.*, 2022, DOI: 10.3390/ijms23042286.
15 Á. M. Nunes, P. Falagan-Lotsch, A. Roslend, M. R. Meneghetti and C. J. Murphy, *Nanoscale Adv.*, 2022, **5**, 733–741.
16 A. Biswas, N. Lemcoff and Y. Weizmann, *Acc. Chem. Res.*, 2025, **58**, 1424–1434.
17 G. Zheng, S. de Marchi, V. López-Puente, K. Sentosun, L. Polavarapu, I. Pérez-Juste, E. H. Hill, S. Bals, L. M. Liz-Marzán, I. Pastoriza-Santos and J. Pérez-Juste, *Small*, 2016, **12**, 3935–3943.
18 M. Tebbe, C. Kuttner, M. Männel, A. Fery and M. Chanana, *ACS Appl. Mater. Interfaces*, 2015, **7**, 5984–5991.
19 A. L. Feng, M. L. You, L. Tian, S. Singamaneni, M. Liu, Z. Duan, T. J. Lu, F. Xu and M. Lin, *Sci. Rep.*, 2015, **5**, 1–10.
20 W. A. Arcos Rosero, A. Bueno Barbezan, C. Daruich de Souza and M. E. Chuery Martins Rostelato, *Pharmaceutics*, 2024, **16**, 255.
21 X. Sun and Y. Li, *Angew. Chem., Int. Ed.*, 2004, **43**, 597–601.
22 W. Gao, X. Wang, H. Fan, Z. Song, X. Lai, Z. Chen and W. Tan, *Sci. Bull.*, 2015, **60**, 1101–1107.
23 Y. V. Kaneti, C. Chen, M. Liu, X. Wang, J. L. Yang, R. A. Taylor, X. Jiang and A. Yu, *ACS Appl. Mater. Interfaces*, 2015, **7**, 25658–25668.
24 K. Bromma and D. B. Chithrani, *Nanomaterials*, 2020, **10**, 1671.
25 G. FRENS, *Nat. Phys. Sci.*, 1973, **241**, 20–22.
26 A. Cohen, M. Alesker, A. Schofield, D. Zitoun and E. Sloutskin, *Gels*, 2016, **2**, 29.
27 Y. Qi, M. Zhang, L. Qi and Y. Qi, *RSC Adv.*, 2016, **6**, 20814–20823.

28 M. Sevilla, C. Sanchís, T. Valdés-Solís, E. Morallón and A. B. Fuertes, *Carbon*, 2008, **46**, 931–939.
29 G. Ischia, M. Cutillo, G. Guella, N. Bazzanella, M. Cazzanelli, M. Orlandi, A. Miotello and L. Fiori, *Chem. Eng. J.*, 2022, **449**, 137827.
30 G. Park, D. Seo, I. S. Chung and H. Song, *Langmuir*, 2013, **29**, 13518–13526.
31 G. Beamson and D. Briggs, *J. Chem. Educ.*, 1993, **70**, A25.
32 F. A. Stevie and C. L. Donley, *J. Vac. Sci. Technol., A*, 2020, DOI: 10.1116/6.0000412.
33 Y. Jun, J.-H. Lee, J. Choi and J. Cheon, *J. Phys. Chem. B*, 2005, **109**, 14795–14806.
34 J. I. Larruquert, L. V. Rodríguez-de Marcos, J. A. Méndez, P. J. Martin and A. Bendavid, *Opt. Express*, 2013, **21**, 27537.
35 X. Fan, W. Zheng and D. J. Singh, *Light Sci. Appl.*, 2014, **3**, 1–14.
36 M. Egorova, A. Tomskaya and S. A. Smagulova, *Materials*, 2023, **16**, 4018.